Modulation of TNAP activity and apatite formation in biomimetic matrix vesicles studied by 31P solid-state NMR

B.Z. Favarin, N. Nassif, T. Azaïs, J. Guignier, S. Mebarek, R. Buchet, J.L. Millán, A.P. Ramos, A.J. Costa-Filho, P. Ciancaglini

Modulation of TNAP activity and apatite formation in biomimetic matrix vesicles studied by ^{31}P solid-state NMR

B.Z. Favarin [a,b,c,*], N. Nassif [c], T. Azaïs [c], J. Guignier [d], S. Mebarek [e], R. Buchet [e], J.L. Millán [f], A.P. Ramos [b], A.J. Costa-Filho [a], P. Ciancaglini [b,**]

[a] Molecular Biophysics Laboratory, Department of Physics, Faculty of Philosophy, Sciences and Letters at Ribeirão Preto, University of São Paulo, Brazil
[b] Department of Chemistry, Faculty of Philosophy, Sciences and Letters at Ribeirão Preto, University of São Paulo, Brazil
[c] Sorbonne Université, CNRS, Laboratoire de Chimie de la Matière Condensée de Paris (LCMCP), F-75005 Paris, France
[d] Sorbonne Université, Institut de Minéralogie et Physique des Milieux Condensés (IMPMC), 4, Place Jussieu, F-75005 Paris, France
[e] Université de Lyon, Université Claude Bernard, Lyon 1, Institut de Chimie et Biochimie Moléculaires et Supramoléculaires, UMR CNRS 5246, UFR de Chimie-Biochimie, F-69622 Villeurbanne, France
[f] Sanford Children's Health Research Center, Sanford Burnham Prebys Medical Discovery Institute, La Jolla, CA 92037, USA

A B S T R A C T

Skeletal and dental mineralization relies on a precisely regulated sequence of events culminating in apatite deposition onto collagen fibrils. Matrix vesicles (MVs), extracellular vesicles released by mineralization-competent cells, play a pivotal role in this process through the catalytic activity of alkaline phosphatase (TNAP). The lipid composition of MVs, particularly phosphatidylserine (PS)-calcium complexes, facilitates the nucleation of amorphous calcium phosphate and apatite formation. However, the interplay between the TNAP structure, the lipid membrane environment, and its enzymatic activity remains incompletely understood.

Biomimetic models of MVs, as proteoliposomes made with dipalmitoylphosphatidylcholine (DPPC) and various TNAP mutants, were used to investigate the TNAP's activity and mineralization potential. Molecular docking and site-directed mutagenesis revealed that specific cysteine substitutions near TNAP's catalytic and anchoring sites influence structural stability, enzymatic activity, and incorporation into lipid bilayers. Notably, TNAP mutants S221C and P307C exhibited enhanced catalytic efficiency in DPPC liposomes, while A420C showed reduced activity due to steric hindrance near the catalytic site. Solid-state NMR and cryo-TEM analyses confirmed hydroxyapatite formation, with significant contributions from lipid-anchored TNAP to the mineralization process.

These findings highlight the critical influence of the lipid environment on TNAP's functional properties and provide insights into the mechanisms governing biomineralization and related pathologies, including hypophosphatasia associated with various TNAP mutations. The study underscores the importance of ATP and pyrophosphate hydrolysis by TNAP in modulating apatite formation and reveals the role of specific TNAP mutations in regulating enzymatic activity, stability, and mineral propagation. Understanding these interactions could lead to alternate therapeutic strategies in treatment and regenerative medicine.

Keywords:
Lipid interface
Biomineralization
Alkaline phosphatase
^{31}P solid-state NMR
Proteoliposome

1. Introduction

Skeletal and dental mineralization involves a precisely controlled series of steps that lead to the organized deposition of calcium and phosphate ions onto collagen fibrils, forming mineral aggregates of apatites ($Ca_{10-x}(HPO_4)_v(CO_3)_w(PO_4)_{6-x}(OH)_{2-x}$ with $x = v + w$, sometimes OH is replaced by Cl^- or F^-). Although the exact mechanism by which the mineral formation occurs remains unknown, matrix vesicles (MVs), a class of matrix-bound extracellular vesicles, are released by mineralization-competent cells like chondrocytes and osteoblasts [1–4]. The MV membrane is enriched in phospholipids, sphingomyelin (SM), and cholesterol (Chol), which closely resemble the compositions of lipid

* Correspondence to: B.Z. Favarin, Molecular Biophysics Laboratory, Department of Physics, Faculty of Philosophy, Sciences and Letters at Ribeirão Preto, University of São Paulo, Brazil.
** Corresponding author.
E-mail addresses: bruno_favarin@hotmail.com (B.Z. Favarin), pietro@ffclrp.usp.br (P. Ciancaglini).

https://doi.org/10.1016/j.bbamem.2025.184446
Received 11 April 2025; Received in revised form 7 August 2025; Accepted 25 August 2025
Available online 27 August 2025

rafts found in parent cell plasma membranes [5,6]. Specifically, the MV membrane contains about 36 % phosphatidylethanolamine (PE), 26.5 % phosphatidylcholine (PC), 3.5 % phosphatidic acid (PA), 7 % phosphatidylinositol (PI), and 16.5 % phosphatidylserine (PS) [7]. The proteome of MVs reveals enrichment in phosphatases and phosphodiesterases like tissue non-specific alkaline phosphatase (TNAP) and ectonucleotide pyrophosphatase/phosphodiesterase (ENPP1), which supports the role of these vesicles in regulating the phosphate (P_i) to pyrophosphate (PP_i) molar ratio during mineralization [8].

One of the critical characteristics of MVs is the presence of a nucleation core in their lumen [8]. The nucleation core consists of a complex formed between amorphous calcium phosphate (ACP) and phosphatidylserine (PS), yielding PS-Ca^{2+} complexes. Amorphous calcium phosphate and lipid-calcium-phosphate complexes (PS-CPLX) containing P_i can generate minerals after incubation with synthetic cartilage lymph (SCL) [8,9]. Although PS-CPLXs containing P_i can induce apatite formation in vivo, many factors seem to regulate its production [10]. PS-CPLXs are present at the early stages in calcifying tissues, including cartilage [11], bone [12], and MVs [13–15].

Mammalian alkaline phosphatases are ectoenzymes anchored to the plasma membrane by a glycosylphosphatidylinositol (GPI) anchor [16]. This GPI motif results from a post-translational modification involving an amino transfer reaction where 29 hydrophobic amino acid residues from the C-terminal are removed, and the GPI anchor is transferred to the Asp484 residue of the new C-terminus of the alkaline phosphatase molecule [17]. There is still a lack of information about the influence of the lipid composition of the membranes on the behavior and activity of GPI-anchored proteins. In 1980, Brasitus and Schanchter found that the biophysical properties of the membrane directly affected the activity of the enzyme 5′- nucleotidase [18]. Subsequent experiments using differential scanning calorimetry (DSC) and polarized fluorescence showed a considerable difference in the structural organization of liposomes in the presence of the enzyme [19] and that its catalytic activity was clearly affected by the physical state of the membrane.

It is well-known that the function of a protein/enzyme depends on its conformation, which in turn is impacted by its direct surroundings (i.e., in solution versus entrapped or under confinement) [20,21]. The catalytic properties of TNAP are indeed dependent on the immediate microenvironment (while on the lipidic membrane or in a soluble form) [22]. Different states of the enzyme (membrane-bound, solubilized with detergent, or solubilized using phospholipase) show specificities for various substrates, suggesting that the kinetic properties of the enzyme are significantly affected by the presence of the GPI anchor and/or other membrane components [23,24]. Garcia et al. [25] reported that GPI-anchored TNAP can give rise to long-reaching modifications that could influence membrane processes halfway through the lipid bilayer. It was concluded that TNAP was probably close to the membrane surface and that this proximity may be related to the modulation of catalytic activity by lipid composition, as previously reported [23,26]. Several strategies have been described to produce MV-mimicking proteoliposomes [23,25,27–31]. We previously reported on the use of TNAP-containing proteoliposomes made of either pure dipalmitoylphosphatidylcholine (DPPC) or DPPC mixed with cholesterol (Chol), sphingomyelin (SM) or both, as MV biomimetic systems to evaluate how the lipid composition and related membrane's physical properties, modulate TNAP incorporation and its catalytic activity. [23,31] Furthermore, incorporating an osteoblast-specific expression model for human TNAP has provided new insights into the enzyme's glycosylation patterns. Glycomic and glycoproteomic analyses revealed that the five N-glycan sites (N140, N230, N271, N303, and N430) are fully occupied by complex-type N-glycans, with core fucosylation predominantly present at all sites except N271. This detailed characterization enriches our understanding of TNAP's structural-functional relationship and its role in bone health. [32]

The current study identified five distinct TNAP regions based on the available placental alkaline phosphatase 3D structure (see materials and methods) for comprehensive molecular docking investigations in membrane models. We purposely targeted mutants containing modifications near the membrane anchoring site and near the catalytic sites to gain insights into the mineralization mechanism of TNAP, and we used ^{31}P solid-state nuclear magnetic resonance (ssNMR) to characterize the final calcium phosphate phases resulting from the post-substrate hydrolysis step. This study explores the connection between enzymatic mutations and disease, focusing on mutations near the catalytic site, which have been the subject of ongoing debate [33] due to their potential impact on enzyme kinetics. Our findings provide insights into mineralization mechanisms by incorporating enzymes into membrane vesicles that closely mimic the biological environment. This approach enhances the understanding of enzymatic mutations and their role in disease pathology.

2. Materials and methods

2.1. Materials

All aqueous solutions were prepared using Millipore DirectQ ultrapure water. Bovine serum albumin (BSA), Trichloroacetic acid (TCA), Tris hydroxymethyl-amino-methane (Tris), 2-amino-2-methyl-propan-1-ol (AMPOL), sodium dodecylsulfate (SDS), *p*-nitrophenyl phosphate disodium salt (pNPP), sodium adenosine-5-triphosphate (ATP), dexamethasone, β-glycerophosphate, polyoxyethylene-9-lauryl ether (polidocanol), dipalmitoylphosphatidylcholine (DPPC), were obtained from Sigma Chemical Co. (St Louis, MO, USA); sodium chloride and magnesium chloride were obtained from Merck (São Paulo, SP, Brazil). 75 cm^2 plastic culture flasks were obtained from Corning (Cambridge, MA, USA). α-MEM, fetal bovine serum, ascorbic acid, gentamicin, and fungizone were obtained from Gibco-Life Technologies (Grand Island, NY, USA). Analytical-grade reagents were used without further purification.

2.2. Site-directed TNAP mutations

The TNAP-encoding pCMV-Script plasmid was previously reported by Millan et al. [16,32,34]. To study the molecular docking mechanisms of TNAP in membrane models [35], five distinct regions of the enzyme that could provide information on molecular interactions with the membrane were chosen based on the PLAP 3D structure (PDB: 1EW2) (Fig. 1). Cysteine (Cys) mutations were selected based on the unique ability of this residue to form disulfide bonds, enabling structural investigations of the protein using techniques such as electron paramagnetic resonance and chemical accessibility assays. The choice of sites to be mutated was based primarily on their proximity to the membrane anchoring region (Pro 307 → Cys), allowing the evaluation of the molecular docking mechanism. In addition, two other mutations in regions close to the membrane but far from the GPI anchoring motif (Pro 263 → Cys and Pro 244 → Cys) were also chosen. Finally, two other regions were selected: one in the intermediacy (Ser 221 → Cys) and another at the opposite end of the anchoring motif (Ala 420 → Cys) located in the crown domain. The oligonucleotides (primers) to change the codon sequence that encodes the target residue were designed following the instructions recommended in the Quikchange manual and with attention to the following requirements: the primers should have a length between 25 and 45 bases, a melting temperature equal to or greater than 78 °C, and the mutation should be in the central portion (Fig. 1).

The amplification was performed by polymerase chain reaction (PCR) using a high-fidelity polymerase KAPA HiFi (KapaBiosystems, Boston, USA). The reaction was prepared using 5 μL of KAPA buffer (5× concentrated), 0.75 μL of dNTP (10 mM stock solution), 1.25 μL of forward primer (100 ng.μL^{-1} stock solution), 1.25 μL of reverse primer (100 ng.μL^{-1} stock solution), 1 μL of template DNA (1–100 ng of DNA), 0.5 μL of KAPA DNA polymerase (1 U/μL), resulting in a final reaction volume of 15.25 μL. At the end of the PCR, 0.5 μL of *Dpn* I enzyme (10 U/

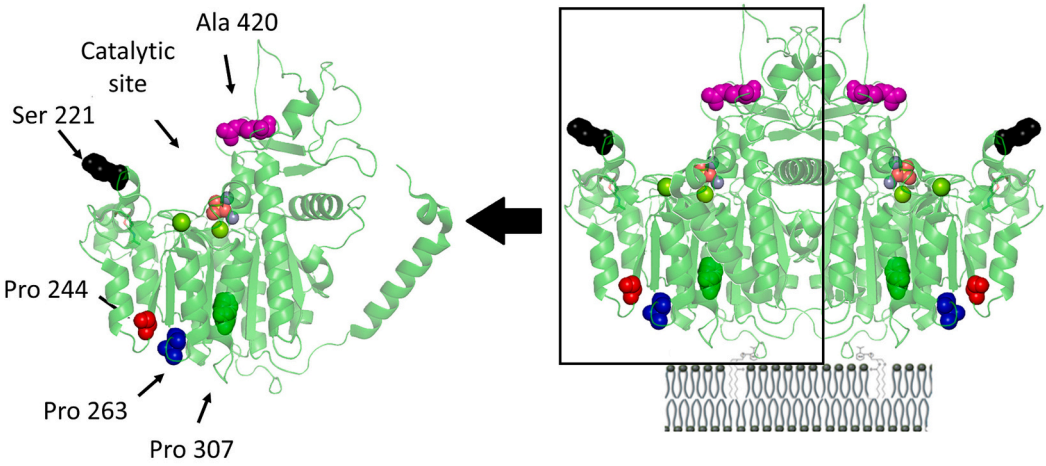

Name	Position of Mutant	Primers 5' – 3'
TNAP wild-Type	--	-
TNAP S221C	Ser 22→Cys	GAT GTG GAG TAT GAG TGT GAC GAG AAA GC
TNAP P244C	Pro 244→Cys	GGA AGA GCT TCA AAT GCA GAT ACA AGC ACT C
TNAP P263C	Pro 263→Cys	CCT GAC CCT TGA CTG CCA CAA TGT G
TNAP P307C	Pro 307→Cys	CCT GCG GAA GAA CTG CAA AGG CTT C
TNAP A420C	Ala 420→Cys	CCA TGG TGG ACT ATT GTC ACA ACA ACT ACC

Fig. 1. Model of the three-dimensional structure of the TNAP monomer constructed based on the crystallographic structure of PLAP (PDB: 1EW2). The regions chosen for site-directed mutations are colored to highlight the changes, indicating the position and residue selected for replacement by cysteine. The crown domain, an important TNAP region, is also indicated in the figure. The name of the mutants is related to the position of the mutation.

μL) and 4 μL of *Dpn* I buffer (5 x concentrated) were added to the reaction. The solution was incubated for 1 h at 37 °C. After digestion of the parental DNA, cells from the XL10-Gold *E. coli* strain (Stratagene, La Jolla, USA) made super-competent by calcium chloride were prepared for transformation by heat shock. To increase the transformation efficiency, 1 μL of β-mercaptoethanol was added to 25 μL of competent cells. This mixture was incubated on ice for 10 min, followed by adding 2 μL of Dpn I-treated mutated DNA. The heat shock transformation protocol was performed as described in the Quikchange manufacturer's manual. The bacteria were plated on LB-agar medium in the presence of kanamycin and incubated for 16 h at 37 °C.

Five transforming colonies of each mutant were inoculated into LB medium and incubated for 16 h at 37 °C. Then, the DNAs were extracted and purified using the EndoFree Plasmid Maxi kit from Qiagen (Germantown, USA), and the fidelity of the mutants was validated by sequencing. The sequencing analysis showed that all the chosen transforming colonies were positive, meaning that all site-directed mutations were successful. Once the sequence integrity of the TNAP mutants was confirmed, the CHO-K1 cells were cultured and subsequently transfected with the plasmids.

The heterologous expression of TNAP and its mutants was performed transiently immediately after cell transfection in a culture medium with 10 % fetal bovine serum in a 144 cm^2 Petri dish. After 24 h of cultured transfected cells in a CO_2 incubator with a saturated atmosphere of 5 % at 37 °C, the culture medium was changed to Opti-MEM, and the expression of the proteins of interest occurred over 30 days of cultivation.

2.3. TNAP expression

CHO-K1 (Chinese hamster ovary, ATCC number CCL-61) cells were trypsinized, and 1.0×10^7 cells were suspended in 800 μL of HEPES-buffered saline containing 10 μg of plasmid of each human TNAP WT or mutant cDNA inserted in the pCMV-Script vector. The cell suspension was placed in an electroporation cuvette (4-mm distance) and electroporated at 400 mV, 250 μF using Gene Pulser (Bio-Rad). After incubation in ice for 20 min, the electroporated cell suspension was diluted ~250 times with growth medium (10 % fetal calf serum, Dulbecco's modified Eagle's medium) and seeded onto 15-cm dishes. Twenty-four hours later, the medium was replaced by the selection medium containing 800 μg/mL G418, and the selection medium was renewed every third day. G418-resistant cells were harvested two weeks later to prepare membrane samples for TNAP [36].

2.4. Solubilization of wild-type human alkaline phosphatase and its mutants

Membrane-bound TNAP was prepared from cultured cells as described previously [37]. Briefly, CHO-K1 cells (ATCC CCL-61) were cultured in α-MEM with 10 % fetal bovine serum until confluence. After trypsinization, 1.0×10^7 cells were electroporated with 10 μg of human TNAP cDNA in the pCMV-Script vector using a Gene Pulser (Bio-Rad). Following incubation on ice and recovery in α-MEM, cells were selected with 0.8 mg/mL G418 for two weeks. G418-resistant cells were harvested for TNAP membrane preparation, following established protocols [23,31]. The enzyme was solubilized with 1 % (v:v) polidocanol, centrifuged at 100,000 ×*g*, and concentrated using an Amicon system.

Protein concentration was determined with SDS [38] and bovine serum albumin as a standard.

Circular dichroism (CD) was used to confirm the secondary structure content of all TNAP expression using a Jasco model J-815 CD Spectrometer (Tokyo, Japan) as previously described in [39].

2.5. Enzymatic activity measurements

p-Nitrophenylphosphate (p-NPP)ase activity was assayed discontinuously at 37 °C by following the liberation of p-nitrophenolate ion (pNP^-) ($\varepsilon_{1M,\ pH13} = 17{,}600\ M^{-1}\ cm^{-1}$) at 410 nm. Standard conditions were 50 mM Tris buffer, pH 7.4, containing 2 mM $MgCl_2$ and 10 mM pNPP in a final volume of 0.5 mL. The reaction was initiated by adding the enzyme and stopped with 0.5 mL of 1 M NaOH at appropriate time intervals [40]. Another quantification used was ATPase, and PP_iase activities were assayed discontinuously by measuring the amount of P_i liberated according to a procedure described previously [41], adjusting the assay medium to a final volume of 0.5 mL. Standard assay conditions were 50 mM Tris buffer, pH 7.4, containing 2 mM $MgCl_2$ and substrate. The reaction was initiated by adding the enzyme, and at appropriate intervals, it was halted by introducing 0.25 mL of cold 30 % trichloroacetic acid (TCA) [41]. All three independent determinations were carried out, and the initial velocities were constant, provided that less than 5 % of the substrate was hydrolyzed. Controls without added enzyme were included in each experiment to allow for the nonenzymatic hydrolysis of substrate. One enzyme unit (1 U) is defined as the amount of enzyme hydrolyzing 1.0 nmol of substrate per minute at 37 °C per milliliter or milligram of protein, as specified in the text. Maximum velocity (V_m), apparent dissociation constant ($K_{0.5}$), and Hill coefficient (n) obtained from substrate hydrolysis were calculated as described previously [26]. Data were reported as the mean of three independent measurements of three different enzyme preparations.

2.6. Liposome and proteoliposome preparation

The lipid DPPC at the appropriate molar ratios (described below) was dissolved in chloroform and dried under nitrogen flow. The resulting lipid film was kept under vacuum overnight and resuspended in 50 mM Tris-HCl buffer, pH 7.5, containing 2 mM $MgCl_2$. The mixture was incubated for 1 h at 60 °C, above the critical phase transition temperature of the lipid, and vortexed for 10 min. Large unilamellar liposomes (LUVs) were prepared by submitting the suspension to extrusion (twenty-one times) through 100 nm polycarbonate membranes in a LiposoFast extrusion system (Liposofast, Sigma-Aldrich). LUVs were prepared and used on the same day. [24]

Membrane-bound TNAP (0.02 mg/mL of total protein) was solubilized with 1 % polidocanol (wt%) (final concentration) for 1 h with constant stirring at 25 °C. To remove excess detergent, 1 mL of polidocanol-solubilized enzyme (~0.05 mg protein/mL) was added to 200 mg of Calbiosorb resin as described [24,36] and the suspension was mixed for 2 h at 4 °C. The supernatant is the source of detergent-free, solubilized enzyme. After detergent removal, this supernatant was used immediately to incorporate TNAP into liposomes to avoid protein aggregation. The protein concentrations present in the liposome were estimated as previously described [36].

2.7. Dynamic light scattering measurements

The determination of liposome and proteoliposome size distribution was performed by dynamic light scattering (DLS) as described elsewhere [23]. The hydrodynamic diameter of the vesicles dispersed in water was obtained at 25 °C by unimodal distribution. The samples were previously filtered (0.8 μm) before measurements. DLS measurements were performed throughout the use of the samples (7 days), and both diameter and intensity varied less than 5 % when stored at 4 °C. Data were reported as the mean of five measurements from three different vesicle preparations.

2.8. Biomineralization assays

The mineralization assay was performed as described by Genge et al. [9] and adapted by Simão et al. [26]. Briefly, the phosphatidylserine (PS) liposomes were prepared by drying 1.25 mg of the lipids in chloroform under an N_2 atmosphere to form a film at the bottom of a test tube. The film was dissolved in 2 mL of intracellular phosphate buffer (ICP) composed of 106.7 mM K^+, 45.1 mM Na^+, 1.5 mM Mg^{2+}, 115.7 mM Cl^-, 23.0 mM P_i, HCO_3^- 10 mM, SO_4^{2-} 1.5 mM and 3.1 mM N_3^-, pH 7.2, and sonicated for 2 min at 25 °C to form small unilamellar liposomes (Concentration of phosphate was relatively high) Propagation of mineral formation was evaluated in the presence of a synthetic nucleation complex made of amorphous calcium phosphate (ACP) combined with PS (PS-CPLX). It was achieved by mixing 1 mL of the PS emulsion previously prepared with 17.5 μL of 100 mM $CaCl_2$ and 1.6 mL of ICP buffer (final calcium concentration was 1,09 mM). This solution was homogenized and centrifuged for 5 min at 15000 ×*g*. The pellet was resuspended in 1 mL of 16.5 mM Tris-HCl buffer, pH 8, and sonicated for 30 s to form an emulsion. At the same time, the synthetic cartilage lymph buffer (SCL) was prepared containing: 2 mM Ca^{2+} and 1 mM ATP as a source of substrate, 104.5 mM Na^+, Cl^- 133.5 mM, sucrose 63.5 mM, 16.5 mM Tris, 12.7 mM K^+, 5.55 mM glucose, 1.83 mM HCO_3^- and 0.57 mM Mg^{2+}. Finally, the mineralization assays were performed in a final volume of 280 μL (in 96 well microplate) where the different liposomes/proteoliposomes (14 μL) were incubated with 140 μL SCL buffer, 21 μL of PS-CPLX suspension, and 14 μL of 16.5 mM Tris-HCl buffer, pH 8 and homogenized for 10 s. The propagation of the mineral was measured by turbidity (absorbance at 340 nm) after 48 h of incubation at 37 °C using a Molecular Devices Microplate Reader M3 [23].

2.9. Cryogenic transmission electron microscopy (Cryo-TEM)

Images were captured using a LaB6 JEOL JEM 2100 cryo-microscope manufactured by JEOL in Japan, operating at 200 kV. The imaging was facilitated by an Ultrascan 1000 CCD camera, a 2 k × 2 k model manufactured by Gatan in the USA. A JEOL low dose system, specifically the Minimum Dose System (MDS), was utilized to minimize irradiation both before imaging to protect the thin ice film and during image capture. The images were recorded at a temperature of 93 K [42].

2.10. Solid-state nuclear magnetic resonance

^{31}P solid-state experiments were conducted on an Avance 300 Bruker spectrometer operating at $\nu(^1H) = 300.13$ MHz and $\nu(^{31}P) = 121.5$ MHz [43]. The samples were packed in 4 mm zirconia rotors and spun at 5 kHz. ^{31}P direct acquisition spectra were used for reference samples (pure ATP, pure DPPC, and pure hydroxyapatite) with a recycle delay (RD) of 60 s and a 30° pulse. The number of scans (NS) was set to 80. The $^1H \rightarrow {}^{31}P$ CP MAS NMR experiments were used for the other samples with RD = 2 s, a contact time (t_{CP}) set at 1 ms, and NS = 2000–8000 scans, depending on the sample. The 2D ^1H-^{31}P HetCor spectra were recorded using the following parameters RD = 2 s; contact time tCP = 1 ms, NS = 32–80 for each 40–120 t_1 increments depending on the sample. The chemical shifts were referenced to H_3PO_4 85 % wt for ^{31}P (0 ppm). [44]

2.11. Transmission electron microscopy (TEM)

For TEM analysis, the samples (~1 mg) were dispersed in ethanol, and some drops were deposited on a lacey carbon film on a copper grid. We used a Philips CM200 FEG transmission electron microscopy, operating at 200 kV, equipped with a field emission gun. Measurements were performed using AnalySIS software (Olympus Soft Imaging Solutions GmbH, Munster, Germany). Measurements of Wber size are reported as the average of direct measurements on each micrograph, and the error is

given as the standard deviation. For measurements of Wber cross-sections that were slightly spherical, the shorter diameter was taken to minimize errors introduced by Wbers that were not directly perpendicular to the section. For measurements of average inter-Wber spacing, Fast Fourier Transforms of square portions of micrographs with relatively uniformly oriented parallel Wbers were calculated in AnalySIS. The intensity proWles were exported and plotted in Microsoft Origin, where the distance between the two peaks corresponding to the spots on the FFT was used to calculate the real space average center-to-center distance between Wbers. Peak positions were hand-picked due to the noisiness of the plots [42,45].

3. Results and discussion

3.1. Heterologous TNAP expression and activity assays

The Far-UV CD spectra indicate that both the WT and mutant TNAPs maintain a similar α-helix-rich secondary structure [46], aligning with the structural profiles typically observed in the majority of alkaline phosphatases documented in the Protein Data Bank [25,46]. This preservation of secondary structure suggests that the cysteine substitutions introduced in the mutants do not disrupt global protein folding or stability, an essential requirement for maintaining enzymatic functionality (Fig. S1).

The activity assay results show a variation in the protein concentration range between 0.179 and 0.196 mg/mL. The specific phosphomonohydrolase activity obtained for WT TNAP was around 600 $U.mg^{-1}$ for the membrane fraction (Table 1). These values are within the expected range, considering both the supernatant and the membrane fraction obtained after ultracentrifugation at 100,000 *g* [23].

The membrane fractions corresponding to the recombinant cells exhibit specific activities in the range of 200 to 500 $U.mg^{-1}$. The highest values for specific phosphomonoesterase activity are observed for TNAP A420C (486.477 $U.mg^{-1}$) and TNAP S221C (480.18 $U.mg^{-1}$). It is worth noting that all the mutant enzymes were solubilized in polidocanol. According to Simao et al. [36], solubilized human WT TNAP has an enzymatic activity of approximately ~700 $U.mg^{-1}$. The comparable activity observed in the cysteine-substituted mutants indicates that their catalytic cores remain functional and structurally intact, even following detergent-mediated solubilization, underscoring their robustness for downstream structural or functional analyses (Fig. S1).

Another important aspect to be considered when working with a protein in solution is its stability and aggregation. The zeta potential of proteins helps predict aggregation. Zeta potentials higher than ±30 mV stand for stable colloidal dispersions [47,48]. Table 1 shows the zeta potential of WT TNAP and the mutants in Tris-HCl buffer (50 mM, pH 7.5) containing $MgCl_2$ (2 mM). All the samples present a negative zeta potential, while larger negative values in the zeta potential modulus for TNAP mutants are observed compared to the wild-type enzyme. This increase in negative surface charge may reflect enhanced electrostatic repulsion among particles, which can mitigate aggregation and contribute to colloidal stability in solution. Additionally, there are no changes in zeta potential for each mutant and wild type in the presence of the lipids (Table 2) or in their absence (Table 1).

The substitution of an amino acid to cysteine (S221C, P244C, P263C, P307C, A420C) maintained TNAP enzymatic activity, but significant differences were observed (Table 3). No signs of inactivation or aggregation in the presence of detergents or liposomes were observed, indicating its structural stability and compatibility with various environments. This highlights the suitability of these variants for membrane-mimetic systems and potential biotechnological applications, where protein stability in amphipathic environments is critical.

Table 1
Amount of protein expressed and zeta potential of the protein solutions (pH: 7.5).

Enzyme name	Protein (mg/mL)	Zeta potential (mV)	V_{max} (U/mg)
TNAP S221C	0.189 ± 0.007	−12.5 ± 1.9	480.2 ± 13.2
TNAP P244C	0.198 ± 0.006	−9.6 ± 1.6	429.6 ± 11.6
TNAP P263C	0.179 ± 0.009	−11.2 ± 1.9	389.7 ± 18.3
TNAP P307C	0.196 ± 0.008	−18.7 ± 1.2	281.8 ± 14.6
TNAP A420C	0.189 ± 0.009	−18.6 ± 1.4	486.5 ± 19.6
TNAP *wild-type*	0.196 ± 0.009	−3.1 ± 1.1	316.7 ± 15.1

Table 2
TNAP and its mutants' incorporation and average diameter of proteoliposomes. Polydispersity values below 0.2 were achieved for both liposomes and proteoliposomes. The data presents the average diameter ± nm derived from triplicates of five distinct preparations. Additionally, it includes the zeta potential of Proteoliposomes at pH 7.4, the quantity of protein integrated into the Proteoliposomes, and the percentage of incorporation relative to the protein amount added to the precursor solution.

Proteoliposome	Diameter (nm)	Zeta potential (mV)	Protein (μg/mL)	Incorporation (%)
DPPC:TNAP wild type[a]	164 ± 10	−8.1 ± 1.9	0.149 ± 0.001	84.8
DPPC:TNAP S221C	157 ± 17	−14.5 ± 2.8	0.139 ± 0.005	78.7
DPPC:TNAP P244C	148 ± 14	−16.6 ± 3.6	0.144 ± 0.006	81.6
DPPC:TNAP P263C	150 ± 16	−14.2 ± 2.6	0.153 ± 0.002	86.7
DPPC:TNAP P307C	138 ± 13	−17.7 ± 2.7	0.148 ± 0.003	83.8
DPPC:TNAP A420C	150 ± 17	−16.6 ± 2.4	0.138 ± 0.004	78.2

[a] Data from reference [23].

3.2. Incorporation of TNAP into membrane models

WT TNAP and TNAP mutants were reconstituted in lipid bilayers to investigate their biochemical properties in a more physiological microenvironment. Phosphatidylcholine is commonly used to reconstitute alkaline phosphatases in liposomes [23]. Moreover, phosphatidylcholine is often selected to investigate the properties of biomembrane models due to their ease of preparation and vesicular stability [49]. Incorporating the protein in liposomes composed by DPPC was carried out using protein-to-lipid molar ratios already standardized in the literature [23]. The formation of the proteoliposomes was followed by DLS (Table 2). As previously shown, no significant changes in the mean hydrodynamic diameter are observed after incorporating WT TNAP or mutants into the bilayers [23]. The values are consistent with previously reported data in the literature for proteoliposomes prepared using WT TNAP, which generally present diameters from 138 to 164 nm. Polydispersion values lower than <0.2 stand for narrow size distributions. The Proteoliposomes with the mutants exhibit higher negative zeta potential values than the native enzyme. The fact that the values are similar to those found for the enzymes in solution (Table 1) supports the presence of the enzyme at the outer layers of the liposomes inserted by the GPI anchor [47,50]. This finding supports proper orientation and anchoring of the protein on the liposomal surface, which is essential for functional accessibility of the catalytic site in membrane environments.

In addition, we observe that, regardless of the position of the substituted cysteine, the amounts of protein incorporated into the liposome are similar; the values of protein concentration are around 0.138–0.153 μg/mL, corresponding to the incorporation of about 78.2–86.8 of the total protein in solution. Similar values were also noticed for the incorporation of WT TNAP [23,27]. These consistent incorporation levels suggest that the introduced mutations do not impair membrane association or insertion via the GPI anchor, reaffirming their structural compatibility with lipid bilayers.

Table 3
Kinetic parameters obtained for ATP hydrolysis by TNAP mutants solubilized or in Proteoliposomes constituted by DPPC.

Enzyme/proteoliposome	Kinetic parameters	Wild-type[a]	S221C	P244C	P263C	P307C	A420C
TNAP solubilized	V_{max} (U/mg)	316.7 ± 15.2[a]	480.2 ± 13.2	429.6 ± 11.6	389.7 ± 18.3	281.8 ± 14.6	486.5 ± 19.6
	$k_{0.5}$ (mM)	0.69 ± 0.01[a]	0.48 ± 0.05	0.63 ± 0.07	0.49 ± 0.09	0.53 ± 0.03	0.56 ± 0.07
	n	1.4 ± 0.2[a]	1.5 ± 0.1	0.9 ± 0.2	1.0 ± 0.2	1.1 ± 0.1	0.8 ± 0.2
	$k_{cat}/K_{0.5}$ ($M^{-1}\cdot s^{-1}$)	9.2×10^2[a]	2.00×10^3	1.40×10^3	1.55×10^3	1.10×10^3	1.02×10^3
DPPC-TNAP	V_{max} (U/mg)	910.0 ± 10.6[a]	1020.9 ± 13.5	914.1 ± 15.2	839.2 ± 13.6	839.3 ± 17.4	614.4 ± 16.6
	$k_{0.5}$ (mM)	3.18 ± 0.02[a]	0.84 ± 0.06	1.08 ± 0.08	1.07 ± 0.07	0.73 ± 0.03	1.34 ± 0.05
	n	3.42 ± 0.1[a]	1.1 ± 0.2	1.1 ± 0.8	1.2 ± 0.6	1.0 ± 0.4	0.9 ± 0.5
	$k_{cat}/K_{0.5}$ ($M^{-1}\cdot s^{-1}$)	5.7×10^2[a]	2.4×10^3	1.7×10^3	1.6×10^3	2.3×10^3	9.1×10^2

[a] Data from reference [27].

3.3. Kinetic characterizations of TNAP mutants

The importance of pyrophosphate and ATP hydrolysis by TNAP in cartilage mineralization and bone formation has been reported [51,52]. The PP_iase and ATPase activities of TNAP decrease the pyrophosphate mineralization inhibitor while a continuous supply of 1–2 mM phosphate from extracellular medium supports mineral nucleation and propagation, thus maintaining a P_i/PP_i ratio which is of importance for regulating the mineralization process [36,53,54]. The kinetic curves obtained from the hydrolysis of ATP by TNAP mutants in solution are depicted in Fig. 2A. Data for WT TNAP in DPPC Proteoliposomes (Vm = 910 U/mg, $K_{0.5}$ = 3.2 mM, n = 3.4, kcat/$K_{0.5}$ = 5.7×10^2 M^{-1} s^{-1}) was published by Favarin [55]. The $K_{0.5}$ values for TNAP mutants are between 0.48 and 0.63 mM, with no significant changes among them. TNAP S221C shows positive cooperativity with an n value of 1.5. The highest V_{max} values are found for TNAP A420C and TNAP S221C with 486.5 U/mg and 480.18 U/mg, respectively, compared to TNAP P244C, TNAP P263C, and TNAP P307C, which have V_{max} values of 429.59, 389.71, and 281.78 U/mg respectively (Table 3). These kinetic differences imply that although global structure is conserved, localized effects from cysteine substitution can influence catalytic turnover potentially via changes in active-site geometry or local flexibility.

The influence of reconstitution into DPPC bilayers on the enzymatic properties of TNAP mutants was evaluated using ATP as a substrate under saturating conditions (Fig. 2B). All variants retained Michaelis–Menten-like kinetics, suggesting proper folding and functional incorporation into the lipid environment. Compared to WT TNAP in DPPC proteoliposomes ($K_{0.5}$ = 1.34 mM), the S221C and P307C mutants exhibited slightly lower $K_{0.5}$ values (0.73 and 0.85 mM, respectively), indicative of increased substrate affinity in the membrane context. Hill coefficients (n) ranged between 0.98 and 1.22 across all variants, pointing to negligible changes in cooperative behavior (Table 3).

Regarding catalytic output, V_{max} values increased slightly upon reconstitution for all constructs. The catalytic efficiency (k_{at}/K_m) of WT TNAP decreased modestly from 1020 to 910 $M^{-1}\cdot s^{-1}$ in DPPC, while P307C exhibited a ~ 2-fold increase in efficiency (from 1200 to 2300 $M^{-1}\cdot s^{-1}$) [23], suggesting that this mutation may enhance performance specifically in the membrane environment. Interestingly, although the absolute efficiency of the A420C mutant remained lower than other variants (1000 $M^{-1}\cdot s^{-1}$), it surpassed WT TNAP in the DPPC context, contrary to what was observed in solution.

Taken together, these data suggest that reconstitution into DPPC proteoliposomes does not compromise catalytic function and that specific cysteine substitutions may subtly modulate enzyme–substrate interactions or conformational dynamics within the bilayer. The membrane environment appears to differentially affect each variant, underscoring the relevance of lipid–protein interactions in determining TNAP functionality.

3.4. Propagation of biomineralization

The ability of Proteoliposomes containing WT TNAP or mutants to propagate mineralization was investigated either in the presence of amorphous phosphate (ACP) or phosphatidylserine-based calcium phosphate complex (PS-CPLX) as nucleators. This protocol differs from others described in the literature [57] as inorganic phosphate (Pi) is not externally supplied; instead, the Pi required for mineral formation is released from ATP hydrolysis catalyzed by TNAP embedded in the membrane [27,50]. This experimental design provides a more biomimetic and controlled environment for evaluating TNAP-mediated mineralization, enabling a direct comparison of how specific structural mutations influence both enzymatic activity and the subsequent nucleation and propagation of hydroxyapatite-like minerals. The ATP concentration used in these assays was optimized based on the kinetic parameters presented in Fig. 2, ensuring substrate saturation. This type of methodological approach has been previously described in the literature for studying enzyme-mediated mineralization under near-physiological conditions. The mineral formation was first investigated for 48 h following the increase in turbidity of free TNAP solutions (i.e., without lipids) containing ATP at 37 °C (Fig. 3). TNAP P244C mutant shows a higher absorbance, which reflected increasing turbidity due to mineral aggregate formation. For S221C, P307C, and A420C mutants, we observe maximum absorbance values of 1.82, 1.19, and 1.03, respectively, while the P263C mutant showed the lowest value (0.43), indicating reduced mineral propagation. The lowest absorbance value is observed for TNAP P263C (0.43). For DPPC proteoliposomes, the lowest absorbance is found for the TNAP P307C mutant. The maximum turbidity values are similar for the other mutants (S221C, P263C, and A420C), i.e., 0.89, 0.94, and 1.09, respectively. The highest mineral propagation is found for the TNAP P244C mutant, which is similar to the data obtained in the solution, followed by the TNAP A420C.

When the same mutants were incorporated into DPPC proteoliposomes and incubated with ATP, the trend in turbidity generally paralleled the data obtained in solution. The P244C mutant again showed the highest turbidity, followed by A420C, S221C, and P263C, with absorbance values of 1.09, 0.89, and 0.94, respectively. The P307C mutant exhibited the lowest turbidity among the liposomal samples. These results indicate that both membrane anchoring and protein conformation modulated by the lipid environment may influence the biomineralization process.

Interestingly, while some mutants (e.g., A420C and P263C) display moderate turbidity in liposomes despite lower turbidity in solution, this suggests that the lipid matrix may partially compensate for the structural effects of certain mutations, highlighting the cooperative role between enzyme structure and membrane context. Furthermore, the agreement between the turbidity data for P244C in both systems reinforces the observation that this mutant is highly effective at promoting mineralization, potentially due to enhanced ATP hydrolysis and efficient nucleation, as supported by the solid-state NMR data described in Section 3.5.

The differences observed in the mineralization efficiency of various mutants in the presence of different phospholipids emphasize the significance of the membrane environment in modulating biomineralization processes. Together with the NMR results, these findings suggest that mutations such as P244C not only preserve the ability to hydrolyze ATP but also enhance the mineral nucleation process, while others,

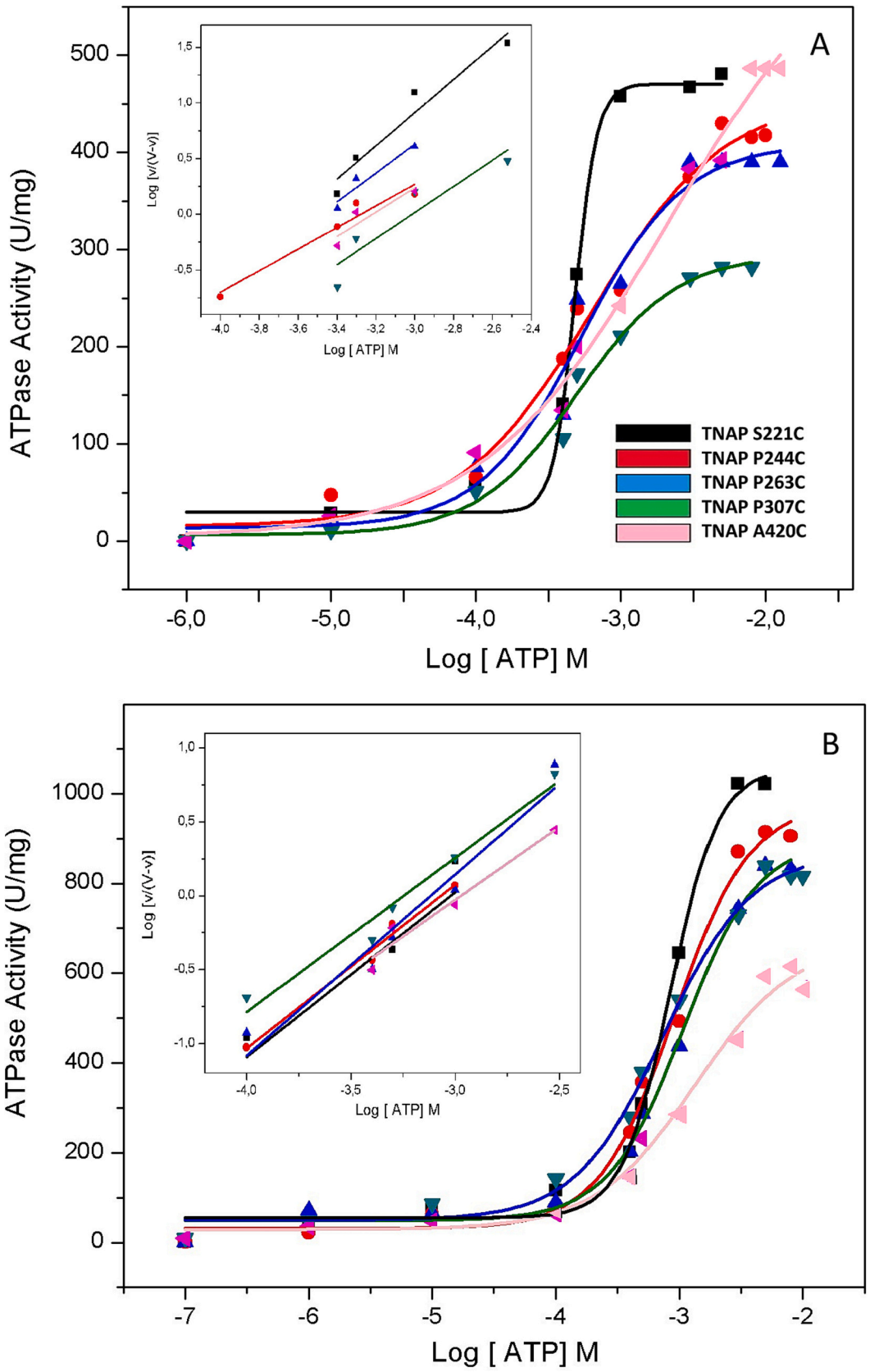

Fig. 2. Effect of ATP concentration on the enzymatic activity of TNAP mutants: (A) solubilized in solution and (B) reconstituted into DPPC liposomes. Enzymatic activity was measured across a range of ATP concentrations. The symbols represent the following TNAP variants: (■) S221C, (●) P244C, (▲) P263C, (▼) P307C, and (◄) A420C. Insets show the corresponding Hill plots illustrating the cooperative binding of ATP for each mutant.

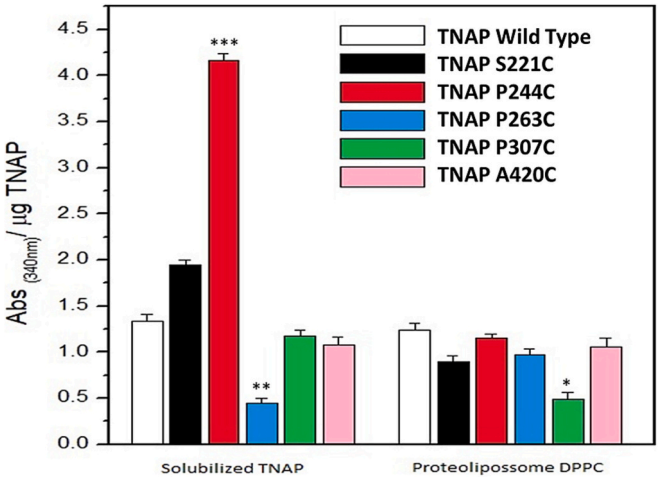

Fig. 3. Effect of TNAP mutants (S221C, P244C, P263C, P307C, and A420C), in both solubilized form and reconstituted into DPPC proteoliposomes, on mineral propagation induced by PS-CPLX–nucleated synthetic cartilage lymph (SCL) at pH 7.5. The assay was performed with a saturating concentration of ATP and incubated for 48 h at 37 °C. Liposomes without enzyme were used as controls. Enzymatic activity is represented as absorbance at 340 nm per µg of TNAP. Data are presented as mean ± SEM from five independent experiments. Statistical significance was assessed using one-way ANOVA; asterisks indicate significant differences compared to wild-type TNAP (*$p < 0.05$, **$p < 0.01$, ***$p < 0.001$).

particularly P263C, may impair one or both steps, depending on their structural impact on the enzyme and its interaction with the lipid membrane.

3.5. *Analysis of the mineral by solid-state NMR–^{31}P CPMAS spectroscopy*

To go deeper into the characterization of our samples, we performed ^{31}P solid-state NMR experiments (Figs. 4 and S2) were performed to probe the nature of precipitated phosphates phases for (i) the complete MVs biomimetic model (i.e., DPPC Proteoliposomes harboring TNAP wild-type using the PS-CPLX nucleator complex after 48 h of incubation in presence of ATP as source of P_i) as well as (ii) to understand the influence of each related constituents on the mineralization process. The ^{31}P solid-state NMR spectra of reference compounds, including ATP (Fig. 4A), DPPC (Fig. 4B), and hydroxyapatite (HAP) (Fig. 4C), were used to define the characteristic spectral regions of each component, highlighted in red for HAP and blue for ATP, thus enabling us to monitor the formation and maturation of mineral phases driven by TNAP activity. ^{31}P solid-state NMR spectra of ATP (Fig. 4A), DPPC (Fig. 4B), and hydroxyapatite (HAP) (Fig. 4C) allow us to define spectral region characteristics of each component (red for HAP, blue for ATP) in order to follow the progress of the HAP mineralization induced by TNP activity. The ^{31}P solid-state NMR spectrum of the PS-CPLX nucleator with ATP indicated broad unresolved bands dominated by ATP (Fig. 4D).

As a result, the ^{31}P solid-state NMR spectrum of HAP is characterized by a single very sharp resonance at 3 ppm (Fig. 4A) as previously reported [58,59]. When all the components are combined to form the complete biomimetic MVs model, the ^{31}P NMR spectrum after 48 h of incubation in the presence of ATP shows a broad resonance centered at ~3 ppm (Fig. 4G), consistent with the formation of crystalline apatite. Notably, the absence of ATP-related signals in this condition indicates complete hydrolysis of ATP by TNAP, confirming enzymatic consumption of the phosphate source to drive mineral formation.

In contrast, when any of the essential components (DPPC, TNAP, or PS-CPLX) is omitted, the formation of crystalline HAP is not observed, and residual ATP signals remain prominent (Fig. 4D–F). This confirms that ATP hydrolysis is a limiting step for mineral propagation and that all components must be present to initiate effective biomineralization.

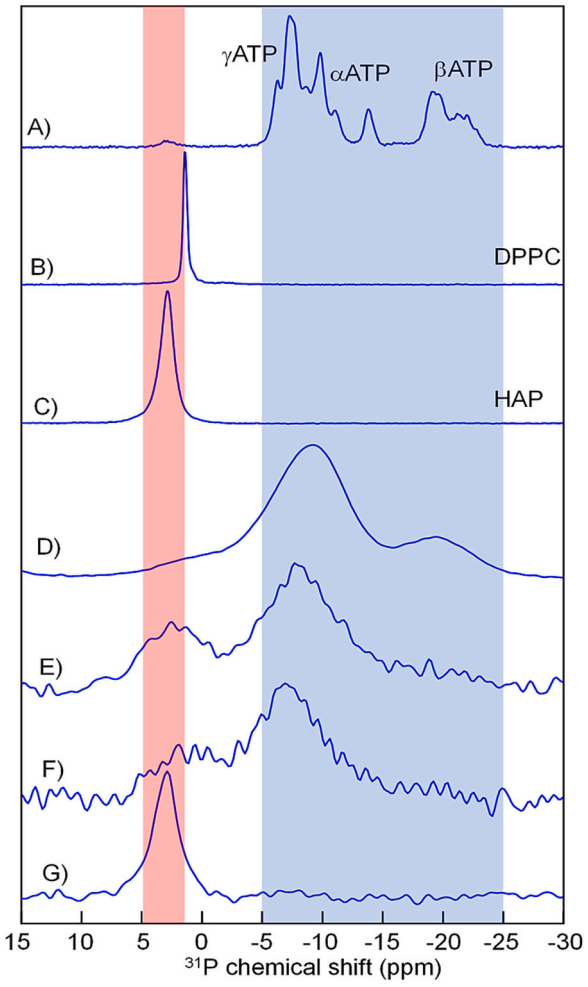

Fig. 4. Solid-state ^{31}P NMR spectra of: A) pure ATP; B) pure DPPC; C) hydroxyapatite reference standard; D) PS-CPLX nucleator incubated with ATP; E) DPPC liposomes containing PS-CPLX nucleator; F) DPPC-proteoliposomes incorporating wild-type TNAP (without PS-CPLX); and G) DPPC-proteoliposomes incorporating wild-type TNAP in the presence of PS-CPLX nucleator (representing the complete biomimetic matrix vesicle model). Samples D–G were incubated with ATP for 48 h to allow sufficient time for mineral propagation and phase transition, mimicking the physiological timeframe of matrix vesicle-mediated biomineralization. Resonance regions corresponding to ATP and hydroxyapatite are highlighted in blue and red, respectively. (For interpretation of the references to color in this figure legend, the reader is referred to the web version of this article.)

Hence, the rate and extent of ATP hydrolysis by membrane-bound TNAP emerge as critical parameters controlling the onset and progression of HAP formation in our model.

The ability of the DPPC proteoliposomes harboring the TNAP mutants to induce mineral propagation was also evaluated by ^{31}P solid-state MAS NMR (Fig. 5). Among the mutant models, the DPPC-TNAP(A420C) mutant was the only one that failed to produce crystalline apatite after incubation with ATP for 48 h, as evidenced by the absence of a peak around 3 ppm (Fig. 5). In contrast, the other mutants exhibit the formation of crystalline apatite (Fig. 5B–E). However, the ^{31}P signals at 3 ppm differ from the WT sample by exhibiting a broader line width. This broadening of the peak is probably related to the presence of apatite and/or other types of minerals, depending on the ATP hydrolysis rate, which influences the type of mineral formed [23,28,31,60].

Indeed, residual ATP (blue zone in Fig. 5) were particularly seen for the mutants A420C and S221C that lacked apatite bands (Fig. 5A) or smaller apatite bands (Fig. 5E) or eventually. These findings reinforce

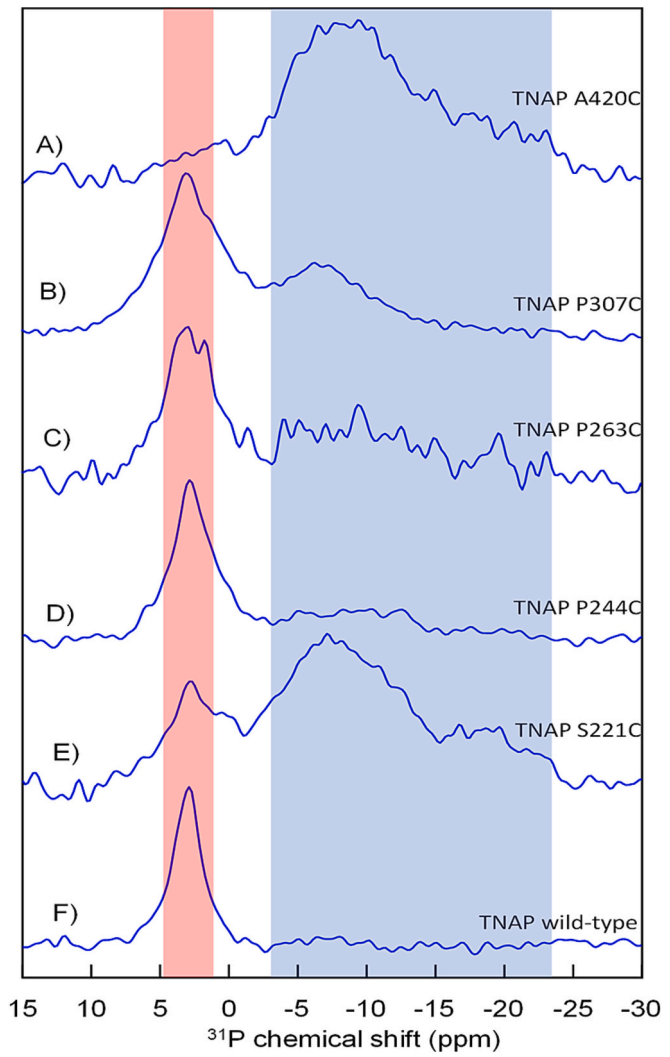

Fig. 5. ^{31}P solid-state NMR spectra of DPPC proteoliposomes harboring TNAP mutants. A) TNAP A420C (active site), B) TNAP P307C (GPI region), C) TNAP P263C (GPI region), D) TNAP P244C (GPI region), E) TNAP S221C (active site), F) TNAP wild-type. All samples were analyzed after 48 h of incubation with ATP in the presence of PS-CPLX nucleator. The spectral regions characteristic of hydroxyapatite and ATP are highlighted in red and in blue, respectively. (For interpretation of the references to color in this figure legend, the reader is referred to the web version of this article.)

the idea that incomplete ATP hydrolysis correlates with impaired mineralization capacity. In contrast, in the P244C mutant, ATP appears to be almost entirely consumed, and the NMR spectrum is dominated by the sharp resonance at 3 ppm, indicating the formation of well-crystallized apatite. When ATP is almost fully hydrolyzed, as in the case of P244C, crystalline apatite is the main phase formed, as seen in the 2D ^{1}H➔^{31}P HetCor NMR spectrum where other mineral complexes are hardly discernable (Fig. S3).

3.6. Cryogenic-transmission electron microscopy (cryo-TEM) of DPPC liposomes containing wild-type TNAP or its mutants

Fig. 6A–B shows a cryo-TEM image of a 10 mg/mL DPPC dispersion without TNAP. DPPC liposomes passed through the 100 nm polycarbonate filter, and the subsequent incorporation of TNAP resulted diverse population of vesicle types, i.e., large and small multivesicular vesicles, oligolamellar vesicles, large and small unilamellar vesicles (Fig. 6A and B). After 24 h of incubation with ATP, the number of liposomes decreases, and electro-dense particles (black dots) mainly located on the membrane are observed. The particles are also observed far from the surface of the liposomes, which indicates that at the time of the study, some membranes are possibly already disrupted, and propagation of mineralization started (Fig. 6C and D). After 48 h of incubation with ATP, it was not possible to identify any structure related to the proteoliposomes. However, particles resembling the granules morphology of hydroxyapatite crystals were observed (Fig. 6E, F, G, H) [61]. These observations are consistent with previous studies showing that lipid membranes can serve as scaffolds or nucleation platforms for the organized formation of calcium phosphate crystals [12,27,62]. In particular, the interaction between phosphatidylserine and calcium ions promotes the formation of mineral precursors, which later develop into crystalline apatite under enzymatically driven conditions.

As a negative control, DPPC liposomes lacking TNAP were also incubated with ATP under identical conditions. As shown in Supplementary Fig. S4, these liposomes did not exhibit any detectable crystal formation, confirming that TNAP is essential for initiating hydroxyapatite nucleation in this biomimetic model. Additional Cryo-TEM analyses were performed for proteoliposomes reconstituted with various TNAP mutants; however, no hydroxyapatite-like crystals were observed under the tested conditions. These findings suggest that crystal formation occurs only under optimal kinetic conditions, achieved with the wild-type TNAP, highlighting that the presence of the enzyme alone is not sufficient. Regardless of variations in kinetic parameters such as V_{max} or $K_{0.5}$, only in the specific enzymatic and membrane context provided by WT TNAP is the nucleation and growth of hydroxyapatite effectively triggered.

3.7. TEM characterization

The morphology of the mineral particles formed after the incubation of DPPC proteoliposomes containing WT TNAP with ATP for 48 h was analyzed using high-resolution transmission electron microscopy (TEM). As illustrated in Fig. 7, agglomerated dense granules with apicular structures (indicated by red arrows in Fig. 7A and B) were observed, suggesting the formation of apatite, which is corroborated by the cryo-TEM images (Fig. 7C) [14]The platelets' dimensions (~10 nm in diameter) were similar to those of apatite minerals found in bone. These apicular and platelet-like hydroxyapatite crystals have also been observed in studies of matrix vesicles derived from chondrocytes and osteoblasts [2,63], supporting that DPPC-based proteoliposomes can mimic key features of biological mineralization.

These results are supported by similar findings from Cruz et al. [14], which also explored apatite formation in MVs. To validate the cryo-TEM findings, the study examined the ability of crude and low-density MVs to induce mineralization at the bulk scale using turbidimetry—a technique widely used to investigate MV mineralization in vitro. For crude MVs (Fig. 6A), there was an initial increase in turbidimetry (absorbance at 350 nm) after a 3-hour lag time, with a 0.3 absorbance unit increase after 8 h of incubation. In contrast, low-density MVs induced slower changes in turbidimetry, with only a 0.1 absorbance unit increase over the same period. [64,65]. These results emphasize the importance of vesicle density, lipid composition, and enzyme activity as determining factors for effective initiation and propagation of mineralization. As a negative control, DPPC liposomes lacking TNAP were also incubated with ATP under identical conditions. As previously discussed, and consistent with the cryo-TEM analysis, no crystals or crystal-like structures were detected in these samples. Therefore, no corresponding structures are shown for these controls in the main figures. Supplementary Fig. 4 confirms the absence of mineralized material, reinforcing the requirement of TNAP activity for initiating hydroxyapatite nucleation in this mimic model.

4. Conclusion

In this work, we privileged mutations of one residue with a cysteine

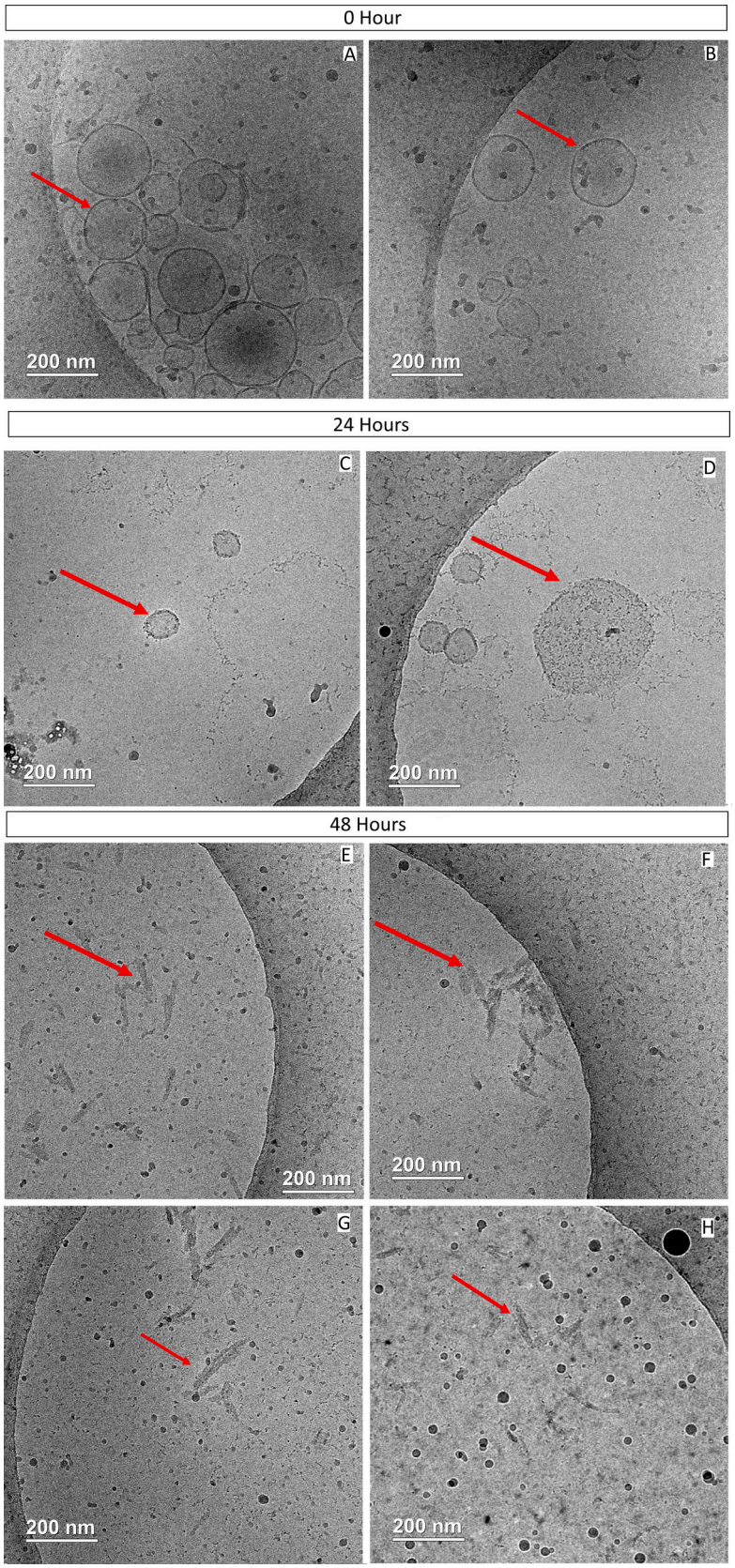

Fig. 6. Cryo-TEM images of DPPC vesicles containing TNAP proteoliposomes after the in vitro biomineralization process. The images show the evolution of the mineralization process over time, from (A and B) 0 to (C and D) 24 h and (E, F, G, H) 48 h. The red arrows indicate the presence of minerals formed during the biomineralization process. (For interpretation of the references to color in this figure legend, the reader is referred to the web version of this article.)

Fig. 7. A and B) Transmission electron microscopy (TEM) images of minerals precipitated after incubation of DPPC proteoliposomes harboring TNAP wild-type 48 h of incubation with ATP.

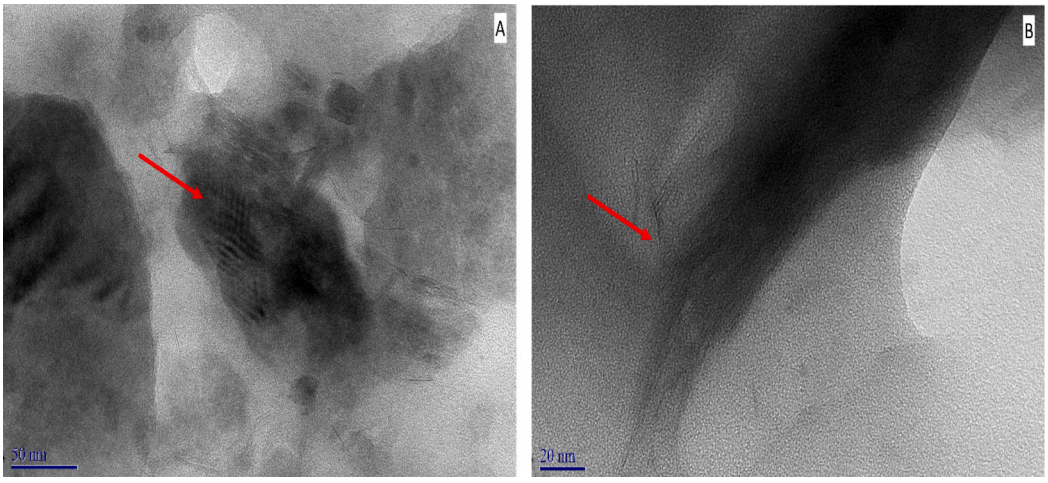

residue with the aim that the free cysteine residue could be chemically labeled with electron paramagnetic resonance or fluorescent maleimide probes. We successfully designed a series of mutants with free cysteine, which retained more or less the phosphatase activity. Indeed, various point mutations of TNAP induced significant effects on the kinetics parameters. A mutation close to the active site is expected to inhibit or significantly impair the activity of TNAP. However, a single mutation in the vicinity of the membrane and far away from the active site, as in P263C and P307C mutants, induced a significant decrease in the Vmax values in the absence of lipids as compared with Vmax values of other mutants. The most striking point is that TNAP anchored in a DPPC model membrane produced additional changes. Indeed, Vmax values were greater for all the mutants inserted in proteoliposomes than those corresponding to free mutants. This observation highlights the crucial role of lipid–protein interactions in modulating enzymatic activity, particularly for GPI-anchored proteins like TNAP. Several studies have demonstrated that the presence of ordered membrane microdomains, such as lipid rafts enriched in cholesterol and sphingolipids, enhances TNAP function by promoting oligomerization or optimal orientation relative to the substrate [3,62]. This supports the accumulated experimental evidence that the activity of TNAP is dependent on its lipidic environment [22–26]. We also analyzed their mineral inducer properties, especially their eventual ability to form mineral aggregates and apatite. For this purpose, ATP, an inhibitor of apatite formation like pyrophosphate, served as a model to monitor mineral formation. Its subsequent hydrolysis by TNAP mutants inserted in proteoliposomes containing PS-CPLX yielded apatite in the cases of wild-type and mutant P244C. However, in the case of mutant A420C, no apatite was observed after 48 h of incubation. Other mutants, including P370C, S221C, and P263C, indicated probably a mixture of apatite and other mineral complexes due to their presence of satellite shoulder in the main apatite peak. These variations suggest that even subtle changes in TNAP structure can profoundly alter its mineralization-inducing capacity. The balance between enzyme kinetics and vesicular localization appears to be a determining factor in the nucleation and propagation of hydroxyapatite crystals. This suggests that a narrow range of TNAP activity is optimum for obtaining apatite within a time frame. From a pathological point of view, it has significant consequences. For instance, hypophosphatasia, a heritable form of rickets and osteomalacia, is caused by loss or weakening function mutations in the *ALPL* gene [66]. 260 mutations have been reported [67] ranging from severe forms characterized by a hypomineralization causing death at or soon after birth. Other cases of hypophosphatasia have high mortality due to respiratory failure caused by undermineralization of ribs. Odonto hypophosphatasia is among the less severe forms and is characterized by dental problems in children and adults. These clinical manifestations underscore the critical need for tightly regulated TNAP activity to ensure proper skeletal development. Enzyme replacement therapy with **asfotase alfa**, a recombinant form of human TNAP modified for bone targeting, has been shown to significantly improve survival and increase bone mineral density in infants with hypophosphatasia [68]. These findings demonstrate that both insufficient and excessive TNAP activity can lead to pathological consequences, emphasizing the value of biomimetic models (such as Proteoliposomes) for investigating the enzyme's functional behavior under controlled conditions. Taken together, this supports that TNAP activity in vivo shall fall in a very narrow range to initiate apatite formation in skeletal tissues optimally. Future studies integrating real-time imaging, single-vesicle assays, and molecular dynamics simulations will be instrumental in elucidating the fine-tuned mechanisms by which TNAP and its lipid microenvironment coordinate the early events of biomineralization.

CRediT authorship contribution statement

B.Z. Favarin: Writing – review & editing, Writing – original draft, Visualization, Validation, Supervision, Software, Resources, Project administration, Methodology, Investigation, Funding acquisition, Formal analysis, Data curation, Conceptualization. **N. Nassif:** Writing – review & editing, Writing – original draft, Supervision, Resources, Methodology. **T. Azaïs:** Writing – review & editing, Resources, Methodology, Investigation, Formal analysis. **J. Guignier:** Investigation, Formal analysis. **S. Mebarek:** Writing – review & editing, Methodology. **R. Buchet:** Writing – review & editing, Investigation, Formal analysis. **J. L. Millán:** Writing – review & editing, Methodology, Formal analysis. **A. P. Ramos:** Writing – review & editing, Writing – original draft, Supervision, Methodology, Investigation, Formal analysis, Data curation, Conceptualization. **A.J. Costa-Filho:** Writing – review & editing, Writing – original draft, Visualization, Validation, Supervision, Resources, Methodology, Investigation, Formal analysis, Data curation, Conceptualization. **P. Ciancaglini:** Writing – review & editing, Writing – original draft, Visualization, Validation, Supervision, Resources, Project administration, Methodology, Investigation, Funding acquisition, Formal analysis, Data curation, Conceptualization.

Funding

The authors acknowledge the funding from: Fundação de Amparo à Pesquisa do Estado de São Paulo (FAPESP), grants 2019/08568-2 (to PC); 2019/25054-2 (to APR); and 2018/12092-0 and 2020/02026-0 (BEPE) (to BZF and AJC); Coordenação de Aperfeiçoamento de Pessoal

de Nível Superior (CAPES) grants Finance Code 001 (to APR and PC); Conselho Nacional de Desenvolvimento Científico e Tecnológico (CNPq) grants 305426/2021-4 (to PC); Brazil-France USP-COFECUB Uc Sv 184/20 grant and grant P01 AG081167 from the National Institute on Aging, National Institutes of Health, USA (to JLM). PC and APR are CNPq researchers.

Declaration of competing interest

The authors declare that they have no known competing financial interests or personal relationships that could have appeared to influence the work reported in this paper.

Data availability

No data was used for the research described in the article.

Appendix A. Supplementary data

Supplementary data to this article can be found online at https://doi.org/10.1016/j.bbamem.2025.184446.

References

[1] M. Bottini, S. Mebarek, K.L. Anderson, A. Strzelecka-Kiliszek, L. Bozycki, A.M. S. Simão, M. Bolean, P. Ciancaglini, J.B. Pikula, S. Pikula, D. Magne, N. Volkmann, D. Hanein, J.L. Millán, R. Buchet, Matrix vesicles from chondrocytes and osteoblasts: their biogenesis, properties, functions and biomimetic models, Biochim. Biophys. Acta (BBA) Gen. Subj. 1862 (2018) 532–546, https://doi.org/10.1016/j.bbagen.2017.11.005.

[2] E.E. Golub, Role of matrix vesicles in biomineralization, Biochim. Biophys. Acta Gen. Subj. 1790 (2009) 1592–1598, https://doi.org/10.1016/j.bbagen.2009.09.006.

[3] J.L. Millán, Alkaline phosphatases, Purinergic Signal 2 (2006) 335, https://doi.org/10.1007/s11302-005-5435-6.

[4] M.C. Yadav, M. Bottini, E. Cory, K. Bhattacharya, P. Kuss, S. Narisawa, R.L. Sah, L. Beck, B. Fadeel, C. Farquharson, J.L. Millán, Skeletal mineralization deficits and impaired biogenesis and function of chondrocyte-derived matrix vesicles in Phospho1−/− and Phospho1/P i t1 double-knockout mice, J. Bone Miner. Res. 31 (2016) 1275–1286, https://doi.org/10.1002/jbmr.2790.

[5] D. Lingwood, K. Simons, Lipid rafts as a membrane-organizing principle, Science 327 (2010) (1979) 46–50, https://doi.org/10.1126/science.1174621.

[6] K. Simons, E. Ikonen, Functional rafts in cell membranes, Nature 387 (1997) 569–572. http://www.ncbi.nlm.nih.gov/pubmed/9177342.

[7] C. Thouverey, A. Strzelecka-Kiliszek, M. Balcerzak, R. Buchet, S. Pikula, Matrix vesicles originate from apical membrane microvilli of mineralizing osteoblast-like Saos-2 cells, J. Cell. Biochem. 106 (2009) 127–138, https://doi.org/10.1002/jcb.21992. http://www.ncbi.nlm.nih.gov/pubmed/19009559.

[8] L.N. Wu, B.R. Genge, D.G. Dunkelberger, R.Z. LeGeros, B. Concannon, R. E. Wuthier, Physicochemical characterization of the nucleational core of matrix vesicles, J. Biol. Chem. 272 (1997) 4404–4411. http://www.ncbi.nlm.nih.gov/pubmed/9020163.

[9] B.R. Genge, L.N. Wu, R.E. Wuthier, In vitro modeling of matrix vesicle nucleation: synergistic stimulation of mineral formation by annexin A5 and phosphatidylserine, J. Biol. Chem. 282 (2007) 26035–26045. http://www.ncbi.nlm.nih.gov/pubmed/17613532 (Epub 2007 Jul 5).

[10] R.E. Wuthier, G.F. Lipscomb, Matrix vesicles: structure, composition, formation and function in calcification, Front. Biosci. (Landmark Ed.) 16 (2011) 2812–2902. http://www.ncbi.nlm.nih.gov/pubmed/21622210.

[11] R.E. Wuthier, Lipids of mineralizing epiphyseal tissues in the bovine fetus, J. Lipid Res. 9 (1968) 68–78. http://www.ncbi.nlm.nih.gov/pubmed/5637432.

[12] A.L. Boskey, A.S. Posner, Extraction of a calcium-phospholipid-phosphate complex from bone, Calcif. Tissue Res. 19 (1976) 273–283. http://www.ncbi.nlm.nih.gov/pubmed/3268.

[13] R.E. Wuthier, S.T. Gore, Partition of inorganic ions and phospholipids in isolated cell, membrane and matrix vesicle fractions: evidence for Ca-Pi-acidic phospholipid complexes, Calcif. Tissue Res. 24 (1977) 163–171. http://www.ncbi.nlm.nih.gov/pubmed/597754.

[14] M. Cruz, F. Van De Loo, E. Macías-Sánchez, A. Akiva, M.A.E. Cruz, L. Rutten, M. Martens, O. Arntz,; Anat Akiva, P. Ciancaglini, A.P. Ramos, N. Sommerdijk, Unravelling the relationship between isolated bone matrix vesicles and forming mineral at the nanometer scale (n.d.). doi:https://doi.org/10.1101/2023.05.09.539570.

[15] I.A. Sheikh, M.T. Midura-Kiela, A. Herchuelz, S. Sokolow, P.R. Kiela, F.K. Ghishan, The Na+/Ca2+ exchanger NCX3 mediates Ca2+ entry into matrix vesicles to facilitate initial steps of mineralization in osteoblasts, J. Extracell. Vesicles 13 (2024), https://doi.org/10.1002/jev2.12450.

[16] M.G. Low, A.R. Saltiel, Structural and functional roles of glycosyl-phosphatidylinositol in membranes, Science 239 (1988) (1979) 268–275, https://doi.org/10.1126/science.3276003.

[17] R. Micanovic, C.A. Bailey, L. Brink, L. Gerber, Y.C. Pan, J.D. Hulmes, S. Udenfriend, Aspartic acid-484 of nascent placental alkaline phosphatase condenses with a phosphatidylinositol glycan to become the carboxyl terminus of the mature enzyme, Proc. Natl. Acad. Sci. 85 (1988) 1398–1402, https://doi.org/10.1073/pnas.85.5.1398.

[18] T.A. Brasitus, D. Schachter, Lipid dynamics and lipid-protein interactions in rat enterocyte basolateral and microvillus membranes, Biochemistry 19 (1980) 2763–2769, https://doi.org/10.1021/bi00553a035.

[19] F.J. Sharom, I. Lorimer, M.P. Lamb, Reconstitution of lymphocyte 5′-nucleotidase in lipid bilayers: behaviour and interaction with concanavalin A, Can. J. Biochem. Cell Biol. 63 (1985) 1049–1057, https://doi.org/10.1139/o85-130.

[20] J. Silvent, M. Robin, C. Bussola Tovani, Y. Wang, F. Soncin, S. Delgado, T. Azaïs, C. Sassoye, M.-M. Giraud-Guille, J.-Y. Sire, N. Nassif, Collagen suprafibrillar confinement drives the activity of acidic calcium-binding polymers on apatite mineralization, Biomacromolecules 22 (2021) 2802–2814, https://doi.org/10.1021/acs.biomac.1c00206.

[21] G.K. Hunter, H.A. Goldberg, Nucleation of hydroxyapatite by bone sialoprotein, Proc. Natl. Acad. Sci. 90 (1993) 8562–8565, https://doi.org/10.1073/pnas.90.18.8562.

[22] P. Ciancaglini, A.M. Simao, F.L. Camolezi, J.L. Millan, J.M. Pizauro, Contribution of matrix vesicles and alkaline phosphatase to ectopic bone formation, Braz. J. Med. Biol. Res. 39 (2006) 603–610. http://www.ncbi.nlm.nih.gov/pubmed/16648897 (Epub 2006 Apr 20).

[23] B.Z. Favarin, M. Bolean, A.P. Ramos, A. Magrini, N. Rosato, J.L. Millan, M. Bottini, A.J. Costa, P. Ciancaglini, Lipid composition modulates ATP hydrolysis and calcium phosphate mineral propagation by TNAP-harboring proteoliposomes, Arch. Biochem. Biophys. 691 (2020) 108482, https://doi.org/10.1016/j.abb.2020.108482.

[24] M. Bolean, A.M. Simao, B.Z. Favarin, J.L. Millan, P. Ciancaglini, Thermodynamic properties and characterization of proteoliposomes rich in microdomains carrying alkaline phosphatase, Biophys. Chem. 158 (2011) 111–118, https://doi.org/10.1016/j.bpc.2011.05.019.

[25] A.F. Garcia, A.M. Simao, M. Bolean, M.F. Hoylaerts, J.L. Millan, P. Ciancaglini, A. J. Costa-Filho, Effects of GPI-anchored TNAP on the dynamic structure of model membranes, Phys. Chem. Chem. Phys. 17 (2015) 26295–26301, https://doi.org/10.1039/c5cp02377g. http://www.ncbi.nlm.nih.gov/pubmed/26389140.

[26] A.M.S. Simão, M. Bolean, M.F. Hoylaerts, J.L. Millán, P. Ciancaglini, Effects of pH on the production of phosphate and pyrophosphate by matrix vesicles' biomimetics, Calcif. Tissue Int. 93 (2013) 222–232, https://doi.org/10.1007/s00223-013-9745-3.

[27] B.Z. Favarin, M.A.R. Andrade, M. Bolean, A.M.S. Simao, A.P. Ramos, M. F. Hoylaerts, J.L. Millan, P. Ciancaglini, Effect of the presence of cholesterol in the interfacial microenvironment on the modulation of the alkaline phosphatase activity during in vitro mineralization, Colloids Surf. B: Biointerfaces 155 (2017) 466–476, https://doi.org/10.1016/j.colsurfb.2017.04.051.

[28] A.M.S. Simão, M. Bolean, B.Z. Favarin, E.A. Veschi, C.B. Tovani, A.P. Ramos, M. Bottini, R. Buchet, J.L. Millán, P. Ciancaglini, Lipid microenvironment affects the ability of proteoliposomes harboring TNAP to induce mineralization without nucleators, J. Bone Miner. Metab. 37 (2019) 607–613, https://doi.org/10.1007/s00774-018-0962-8.

[29] J. Gastaldi Cominal, H. Gobbi Sebinelli, L. Hayann, L. Fabrício Bahia Nogueira, M. Antonio Eufrásio Cruz, M. Trafanni Mello, L. Henrique da Silva Andrilli, M. Bolean, A. Paula Ramos, S. Mebarek, M. Bottini, J. Luis Millán, P. Ciancaglini, J. Luis Millan, A protein corona modulates the function of mineralization-competent matrix vesicles, JBMR Plus 9 (2025), https://doi.org/10.1093/jbmrpl/ziae168/7931791.

[30] M. Balcerzak, E. Hamade, L. Zhang, S. Pikula, G. Azzar, J. Radisson, J. Bandorowicz-Pikula, R. Buchet, M. Nencki, The Roles of Annexins and Alkaline Phosphatase in Mineralization Process, n.d.

[31] L.H.S. Andrilli, H.G. Sebinelli, B.Z. Favarin, M.A.E. Cruz, A.P. Ramos, M. Bolean, J. L. Millan, M. Bottini, P. Ciancaglini, NPP1 and TNAP hydrolyze ATP synergistically during biomineralization, Purinergic Signal. (2022), https://doi.org/10.1007/s11302-022-09882-2.

[32] D. Atanasova, E. Mirgorodskaya, L. Moparthi, S. Koch, M. Haarhaus, S. Narisawa, J.L. Millán, E. Landberg, P. Magnusson, Glycoproteomic profile of human tissue-nonspecific alkaline phosphatase expressed in osteoblasts, JBMR Plus 8 (2024), https://doi.org/10.1093/jbmrpl/ziae006.

[33] A.E. Beattie, S.D. Gupta, L. Frankova, A. Kazlauskaite, J.M. Harmon, T.M. Dunn, D. J. Campopiano, The pyridoxal 5′-phosphate (PLP)-dependent enzyme serine palmitoyltransferase (SPT): effects of the small subunits and insights from bacterial mimics of human hLCB2a HSAN1 mutations, Biomed. Res. Int. 2013 (2013), https://doi.org/10.1155/2013/194371.

[34] J.L. Millán, M.P. Whyte, Alkaline phosphatase and hypophosphatasia, Calcif. Tissue Int. 98 (2016) 398–416, https://doi.org/10.1007/s00223-015-0079-1.

[35] Y. Yu, K. Rong, D. Yao, Q. Zhang, X. Cao, B. Rao, Y. Xia, Y. Lu, Y. Shen, Y. Yao, H. Xu, P. Ma, Y. Cao, A. Qin, The structural pathology for hypophosphatasia caused by malfunctional tissue non-specific alkaline phosphatase, Nat. Commun. 14 (2023) 4048, https://doi.org/10.1038/s41467-023-39833-3.

[36] A.M. Simao, M.C. Yadav, P. Ciancaglini, J.L. Millan, Proteoliposomes as matrix vesicles' biomimetics to study the initiation of skeletal mineralization, Braz. J. Med. Biol. Res. 43 (2010) 234–241. http://www.ncbi.nlm.nih.gov/pubmed/20401430.

[37] A.M. Simao, M.M. Beloti, R.M. Cezarino, A.L. Rosa, J.M. Pizauro, P. Ciancaglini, Membrane-bound alkaline phosphatase from ectopic mineralization and rat bone marrow cell culture, Comp. Biochem. Physiol. A Mol. Integr. Physiol. 146 (2007) 679–687. http://www.ncbi.nlm.nih.gov/pubmed/16798036 (Epub 2006 May 20).
[38] E.F. Hartree, Determination of protein: a modification of the Lowry method that gives a linear photometric response, Anal. Biochem. 48 (1972) 422–427. http://www.ncbi.nlm.nih.gov/pubmed/4115981.
[39] M.-H. Le Du, J.L. Millán, Structural evidence of functional divergence in human alkaline phosphatases, J. Biol. Chem. 277 (2002) 49808–49814, https://doi.org/10.1074/jbc.M207394200.
[40] J.M. Pizauro, P. Ciancaglini, F.A. Leone, Characterization of the phosphatidylinositol-specific phospholipase C-released form of rat osseous plate alkaline phosphatase and its possible significance on endochondral ossification, Mol. Cell. Biochem. 152 (1995) 121–129. http://www.ncbi.nlm.nih.gov/pubmed/8751158.
[41] T. Kiffer-Moreira, C.R. Sheen, K.C. da S. Gasque, M. Bolean, P. Ciancaglini, A. van Elsas, M.F. Hoylaerts, J.L. Millán, Catalytic signature of a heat-stable, chimeric human alkaline phosphatase with therapeutic potential, PLoS One 9 (2014) e89374, https://doi.org/10.1371/journal.pone.0089374.
[42] J.J. De Yoreo, S.N.A. J. M., Investigating materials formation with liquid-phase and cryogenic TEM, Nat. Rev. Mater. 1 (2016) 16035, https://doi.org/10.1038/natrevmats.2016.35.
[43] T. Azais, L. Bonhomme-Coury, J. Vaissermann, P. Bertani, J. Hirschinger, J. Maquet, C. Bonhomme, Synthesis and characterization of a novel cyclic aluminophosphinate: structure and solid-state NMR study, Inorg. Chem. 41 (2002) 981–988, https://doi.org/10.1021/ic010700k.
[44] D. Aiello, N. Folliet, G. Laurent, F. Testa, C. Gervais, F. Babonneau, T. Azaïs, Solid state NMR characterization of phenylphosphonic acid encapsulated in SBA-15 and aminopropyl-modified SBA-15, Microporous Mesoporous Mater. 166 (2013) 109–116, https://doi.org/10.1016/j.micromeso.2012.04.028.
[45] G.M.L. Dalmônico, D. Ihiawakrim, N. Ortiz, A.G. Barreto Junior, C.F. Curitiba Marcellos, M. Farina, O. Ersen, A.L. Rossi, Live visualization of the nucleation and growth of needle-like hydroxyapatite crystals in solution by in situ TEM, Cryst. Growth Des. 22 (2022) 4828–4837, https://doi.org/10.1021/acs.cgd.2c00296.
[46] N.J. Greenfield, Using circular dichroism spectra to estimate protein secondary structure, Nat. Protoc. 1 (2006) 2876, https://doi.org/10.1038/NPROT.2006.202.
[47] A.H. Weerkamp, H.M. Uyen, H.J. Busscher, Effect of zeta potential and surface energy on bacterial adhesion to uncoated and saliva-coated human enamel and dentin, J. Dent. Res. 67 (1988) 1483–1487, https://doi.org/10.1177/00220345880670120801.
[48] A.A. Chaudhry, H. Yan, K. Gong, F. Inam, G. Viola, M.J. Reece, J.B. Goodall, I. ur Rehman, F.K. McNeil-Watson, J.C. Corbett, J.C. Knowles, J.A. Darr, High-strength nanograined and translucent hydroxyapatite monoliths via continuous hydrothermal synthesis and optimized spark plasma sintering, Acta Biomater. 7 (2011) 791–799, https://doi.org/10.1016/j.actbio.2010.09.029.
[49] M. Bolean, A.M. Simao, B.Z. Favarin, J.L. Millan, P. Ciancaglini, The effect of cholesterol on the reconstitution of alkaline phosphatase into liposomes, Biophys. Chem. 152 (2010) 74–79, https://doi.org/10.1016/j.bpc.2010.08.002.
[50] S. Sesana, F. Re, A. Bulbarelli, D. Salerno, E. Cazzaniga, M. Masserini, Membrane features and activity of GPI-anchored enzymes: alkaline phosphatase reconstituted in model membranes, Biochemistry 47 (2008) 5433–5440, https://doi.org/10.1021/bi800005s. http://www.ncbi.nlm.nih.gov/pubmed/18416535 (Epub 2008 Apr 17).
[51] L.N. Wu, T. Yoshimori, B.R. Genge, G.R. Sauer, T. Kirsch, Y. Ishikawa, R. E. Wuthier, Characterization of the nucleational core complex responsible for mineral induction by growth plate cartilage matrix vesicles, J. Biol. Chem. 268 (1993) 25084–25094. http://www.ncbi.nlm.nih.gov/pubmed/8227072.
[52] H.H. Hsu, H.C. Anderson, The deposition of calcium pyrophosphate by NTP pyrophosphohydrolase of matrix vesicles from fetal bovine epiphyseal cartilage, Int. J. Biochem. 18 (1986) 1141–1146. http://www.ncbi.nlm.nih.gov/pubmed/3028885.
[53] J.L. Millán, The role of phosphatases in the initiation of skeletal mineralization, Calcif. Tissue Int. 93 (2013) 299–306, https://doi.org/10.1007/s00223-012-9672-8.
[54] G.W. Cyboron, R.E. Wuthier, Purification and initial characterization of intrinsic membrane-bound alkaline phosphatase from chicken epiphyseal cartilage, J. Biol. Chem. 256 (1981) 7262–7268. http://www.ncbi.nlm.nih.gov/pubmed/7251597.
[55] W. Querido, ad Shanas, S. Bookbinder, M. Cecilia Oliveira-Nunes, B. Krynska, N. Pleshko, Fourier transform infrared spectroscopy of developing bone mineral: from amorphous precursor to mature crystal, (n.d.). doi:https://doi.org/10.1039/c9an01588d.
[57] R.E. Wuthier, J.E. Chin, J.E. Hale, T.C. Register, L.V. Hale, Y. Ishikawa, Isolation and characterization of calcium-accumulating matrix vesicles from chondrocytes of chicken epiphyseal growth plate cartilage in primary culture, J. Biol. Chem. 260 (1985) 15972–15979. http://www.ncbi.nlm.nih.gov/pubmed/3905800.
[58] N. Nassif, F. Martineau, O. Syzgantseva, F. Gobeaux, M. Willinger, T. Coradin, S. Cassaignon, T. Azaïs, M.M. Giraud-Guille, In vivo inspired conditions to synthesize biomimetic hydroxyapatite, Chem. Mater. 22 (2010) 3653–3663, https://doi.org/10.1021/cm903596q.
[59] Y. Wang, S. Von Euw, G. Laurent, C. Crevant, L. Bonhomme-Coury, M.M. Giraud-Guille, F. Babonneau, N. Nassif, T. Azaïs, Impact of collagen confinement vs. ionic substitutions on the local disorder in bone and biomimetic apatites, Mater. Horiz. 1 (2014) 224–231, https://doi.org/10.1039/c3mh00071k.
[60] A.P. Ramos, M. Bolean, M.A.E. Cruz, L.H.S. Andrilli, L.F.B. Nogueira, H. G. Sebinelli, A.L.N. Dos Santos, B.Z. Favarin, J.M.M. Macedo, E.A. Veschi, C. R. Ferreira, J.L. Millan, M. Bottini, P. Ciancaglini, Langmuir monolayers and proteoliposomes as models of matrix vesicles involved in biomineralization, Biophys. Rev. 13 (2021) 893–895, https://doi.org/10.1007/s12551-021-00866-x.
[61] T. Schaffran, J. Li, G. Karlsson, K. Edwards, M. Winterhalter, D. Gabel, Interaction of N,N,N-trialkylammonioundecahydro-closo-dodecaborates with dipalmitoyl phosphatidylcholine liposomes, Chem. Phys. Lipids 163 (2010) 64–73, https://doi.org/10.1016/j.chemphyslip.2009.09.004.
[62] S. Narisawa, M.C. Yadav, J.L. Millán, In vivo overexpression of tissue-nonspecific alkaline phosphatase increases skeletal mineralization and affects the phosphorylation status of osteopontin, J. Bone Miner. Res. 28 (2013) 1587–1598, https://doi.org/10.1002/jbmr.1901.
[63] A. Lotsari, A.K. Rajasekharan, M. Halvarsson, M. Andersson, Transformation of amorphous calcium phosphate to bone-like apatite, Nat. Commun. 9 (2018) 4170, https://doi.org/10.1038/s41467-018-06570-x.
[64] M.J. Glimcher, The nature of the mineral component of bone and the mechanism of calcification, Instr. Course Lect. 36 (1987) 49–69.
[65] J. Hamada, K. Tamai, W. Ono, K. Saotome, Does the nature of deposited basic calcium phosphate crystals determine clinical course in calcific periarthritis of the shoulder? J. Rheumatol. 33 (2006) 326–332.
[66] M.J. Weiss, D.E. Cole, K. Ray, M.P. Whyte, M.A. Lafferty, R.A. Mulivor, H. Harris, A missense mutation in the human liver/bone/kidney alkaline phosphatase gene causing a lethal form of hypophosphatasia, Proc. Natl. Acad. Sci. 85 (1988) 7666–7669, https://doi.org/10.1073/pnas.85.20.7666.
[67] M.P. Whyte, Physiological role of alkaline phosphatase explored in hypophosphatasia, Ann. N. Y. Acad. Sci. 1192 (2010) 190–200, https://doi.org/10.1111/j.1749-6632.2010.05387.x.
[68] M.P. Whyte, C.R. Greenberg, N.J. Salman, M.B. Bober, W.H. McAlister, D. Wenkert, B.J. Van Sickle, J.H. Simmons, T.S. Edgar, M.L. Bauer, M.A. Hamdan, N. Bishop, R. E. Lutz, M. McGinn, S. Craig, J.N. Moore, J.W. Taylor, R.H. Cleveland, W. R. Cranley, R. Lim, T.D. Thacher, J.E. Mayhew, M. Downs, J.L. Millán, A. M. Skrinar, P. Crine, H. Landy, Enzyme-replacement therapy in life-threatening hypophosphatasia, N. Engl. J. Med. 366 (2012) 904–913, https://doi.org/10.1056/NEJMoa1106173.